Seasonal Variation of the Pacific South Equatorial Current Bifurcation

ZHAOHUI CHEN AND LIXIN WU

Physical Oceanography Laboratory/Qingdao Collaborative Innovation Center of Marine Science and Technology, Ocean University of China, Qingdao, China

(Manuscript received 27 April 2014, in final form 9 April 2015)

ABSTRACT

The seasonal variation of the South Equatorial Current (SEC) bifurcation off the Australian coast in the South Pacific (SP) is investigated with observations and a nonlinear, reduced-gravity, primitive equation model of the upper ocean. The mean SEC bifurcation latitude (SBL) integrated over the upper thermocline is around 17.5°S, almost 2° south of the position predicted by Sverdrup theory. For its seasonal variation, the SBL reaches its southernmost position in June/July and its northernmost position in November/December. The south–north migration of 2.7° is twice as large as its counterpart in the North Pacific. It is found that the large seasonal amplitude of the SBL results from the combined effect of Low-Lat-SP and Non-Low-Lat-SP processes. The Low-Lat-SP process (referred to as the Rossby wave dynamics forced by the wind stress curl over the low-latitude SP) accounts for almost $^2/_3$ of the SBL seasonal variability, and the Non-Low-Lat-SP processes account for $^1/_3$. Both of these processes are responsible for its south–north migration but in different ways. The Low-Lat-SP wind forcing determines the offshore upper-layer thickness (ULT) via Rossby wave propagation, while the Non-Low-Lat-SP wind forcing determines the alongshore ULT via coastal Kelvin wave propagation. A simple bifurcation model is proposed under the framework of linear Rossby wave dynamics. It is found that the seasonal bifurcation latitude is predominantly determined by the spatial pattern of the wind and baroclinic Rossby wave propagation. This model explains the roles of local/remote wind forcing and baroclinic adjustment in the south–north migration and peak seasons of the bifurcation latitude.

1. Introduction

The South Equatorial Current (SEC), the northern limb of the subtropical gyre in the South Pacific (SP), flows approximately between 5°N and 20°S (Ganachaud et al. 2007). It is propelled westward by the southeast trade winds and finally breaks into multiple zonal jets, which flow primarily through the gap between New Caledonia and the Solomon Islands as it enters the Coral Sea (e.g., Webb 2000; Gourdeau et al. 2008). After encountering the Australian coast, the jets split into two western boundary currents, that is, the equatorward Gulf of the Papua Current (GPC; e.g., Burrage et al. 2012; Kessler and Cravatte 2013) and poleward East Australian Current (EAC; e.g., Ridgway and Dunn 2003), both of which are believed to be crucial to the downstream dynamical environment (e.g., Tsuchiya et al. 1989; Ridgway and Godfrey 1997).

As the origin of the low-latitude western boundary currents, the bifurcation of this equatorial current plays significant roles in redistributing water mass and heat meridionally. In the SP, in-depth studies of the SEC bifurcation latitude (SBL) have been intensively conducted over the last two decades both in observations and in modeling studies (e.g., Church 1987; De Szoeke 1987; Qu and Lindstrom 2002; Kessler and Gourdeau 2007; Kessler and Cravatte 2013). Most of these studies, however, only focused on the vertical structure of the SEC bifurcation at the western boundary; its seasonal variations have rarely been explored. Therefore, a systematic study of its seasonal cycle and the relevant dynamics are required to deepen our understanding of the SP ocean circulation. This is also a key scientific issue of the Southwest Pacific Ocean Circulation and Climate Experiment (Ganachaud et al. 2007).

In the North Pacific (NP), there have been numerous studies focusing on the seasonal variation of the North Equatorial Current (NEC) bifurcation latitude (NBL) off the Philippine coast (e.g., Qiu and Lukas 1996; Qu and Lukas 2003; Kim et al. 2004; Wang and Hu 2006; Jensen 2011; Chen and Wu 2011, 2012). These studies

Corresponding author address: Zhaohui Chen, Physical Oceanography Laboratory, Ocean University of China, 5 Yushan Road, Qingdao 266003, China.
E-mail: chenzhaohui@ouc.edu.cn

DOI: 10.1175/JPO-D-14-0085.1

clarified that the NEC bifurcation is most prominent in the upper-layer ocean and that wind forcing with baroclinic adjustment is responsible for its seasonal variation in terms of the south–north migration A_b and peak seasons. Compared with its Northern Hemisphere counterpart, the bifurcation off the Australian coast is more complicated. In particular, previous studies have shown that the Indonesian Throughflow (ITF) can shift the mean bifurcation latitude southward relative to the prediction of Sverdrup theory (Qu and Lindstrom 2002; McCreary et al. 2007); the complex topography in the western boundary (i.e., the shallow Queensland Plateau) makes it difficult to distinguish the real position of the bifurcation (Kessler and Cravatte 2013), and the island obstacles to the incoming SEC lead to modifications on inflows before reaching the western boundary (Webb 2000; Gourdeau et al. 2008; Couvelard et al. 2008). The above factors may have an effect on obtaining the accurate location of the bifurcation but will not pose a serious problem in depicting the overall pattern of its seasonal cycle. In this study, therefore, attention will be paid to the seasonal variation of the SBL averaged in the upper-layer ocean and its comparison with the NEC bifurcation.

This paper is organized as follows: Section 2 describes the data and methodology, followed by a general description of the SBL seasonal variation in section 3. In section 4, the roles of Low-Lat-SP processes, like Rossby wave propagation, and Non-Low-Lat-SP processes, like alongshore winds, are discussed in detail. A simple bifurcation model is presented in section 5. Section 6 provides a summary and further discussions.

2. Data and methods

The World Ocean Database 2009 (WOD09) of the National Oceanographic Data Center (NODC) is used to construct the monthly climatological temperature and salinity fields in the region 40°S–0°, 140°E–180° (Boyer et al. 2009). Before obtaining the gridded data from the profiles, we first plot the spatial and temporal distributions of available profiles in Figs. 1a and 1b. They are not uniformly distributed; most profiles are confined to the southeast coast of Australia, in the east of New Caledonia and around the Solomon Islands, but they suffice to get a general map of the temperature–salinity (T–S) field. The vertical and monthly distributions of the available profiles (Figs. 1c,d) indicate that the data are mainly concentrated in the upper 400 m without significant seasonal biases, ensuring that the seasonal variation of the upper-layer bifurcation can be reliably derived from this dataset.

The T–S data are interpolated into a monthly field in a three-dimensional grid; the quality-controlled T–S data are first interpolated onto a 10-m vertical grid between the surface and 1200 m, then the T–S values are mapped onto a 0.5° by 0.5° grid using an objective mapping technique at each depth. Unlike the spatial decorrelation scale used in Qiu et al. (2013), here we adopt $L_x = 0.5°$ in longitude and $L_y = 0.5°$ in latitude in the Gaussian weight function form of $\exp[-\Delta x^2/(2L_x^2) - \Delta y^2/(2L_y^2)]$ to ensure a high weight of the observations within the western boundary current regions. The gridded monthly data are then smoothed horizontally using a two-dimensional Gaussian filter with an e-folding scale of 0.5° to reduce the noise produced by small-scale motions like internal waves and tides. Finally, the T–S fields are converted to dynamic heights with the reference level at 1200 m, and the geostrophic velocities are subsequently derived. Here, we choose 1200 m as the reference level owing to the lack of T–S observations beneath this depth, although it is suggested by Kessler and Cravatte (2013) that there is no appropriate ''level of no motion'' in the Coral Sea.

In addition to WOD09, the global sea surface height (SSH) anomaly dataset that merges the Ocean Topography Experiment (TOPEX)/Poseidon, *European Remote Sensing Satellite 1* and *2* (*ERS-1* and *ERS-2*), *Geosat Follow-On*, and *Jason-1* and *Jason-2* along-track SSH measurements. The dataset has a weekly format on a 1/3° × 1/3° Mercator grid and covers the period from January 1993 to December 2012. The weekly dataset is then temporally averaged to form the monthly SSH anomaly dataset in this study. Following the method of Chen et al. (2014), the surface SBL can be derived from the meridional geostrophic velocity using the SSH anomaly in combination with the hybrid mean dynamic topography by Rio et al. (2011). We also employ a recently developed Estimating the Circulation and Climate of the Ocean, Phase II (ECCO2), product, which aims to produce an accurate synthesis of all available global-scale ocean and sea ice data that resolve ocean eddies and other narrow current systems (Menemenlis et al. 2008). ECCO2 provides monthly zonal and meridional velocities with high spatial resolution (1/4° × 1/4°) to adequately diagnose the seasonal cycle of circulation in the western boundary current system, particularly the bifurcation off the Australian coast. In addition, the ERA-Interim wind stress that spans from 1979 to 2012 is used to force the models in this study.

3. Seasonal cycle of the upper-layer SBL off the Australian coast

a. Mean SBL and its seasonal cycle

The depth-integrated (0–400 m) dynamic height and upper-layer mean geostrophic flow are shown in Fig. 2a.

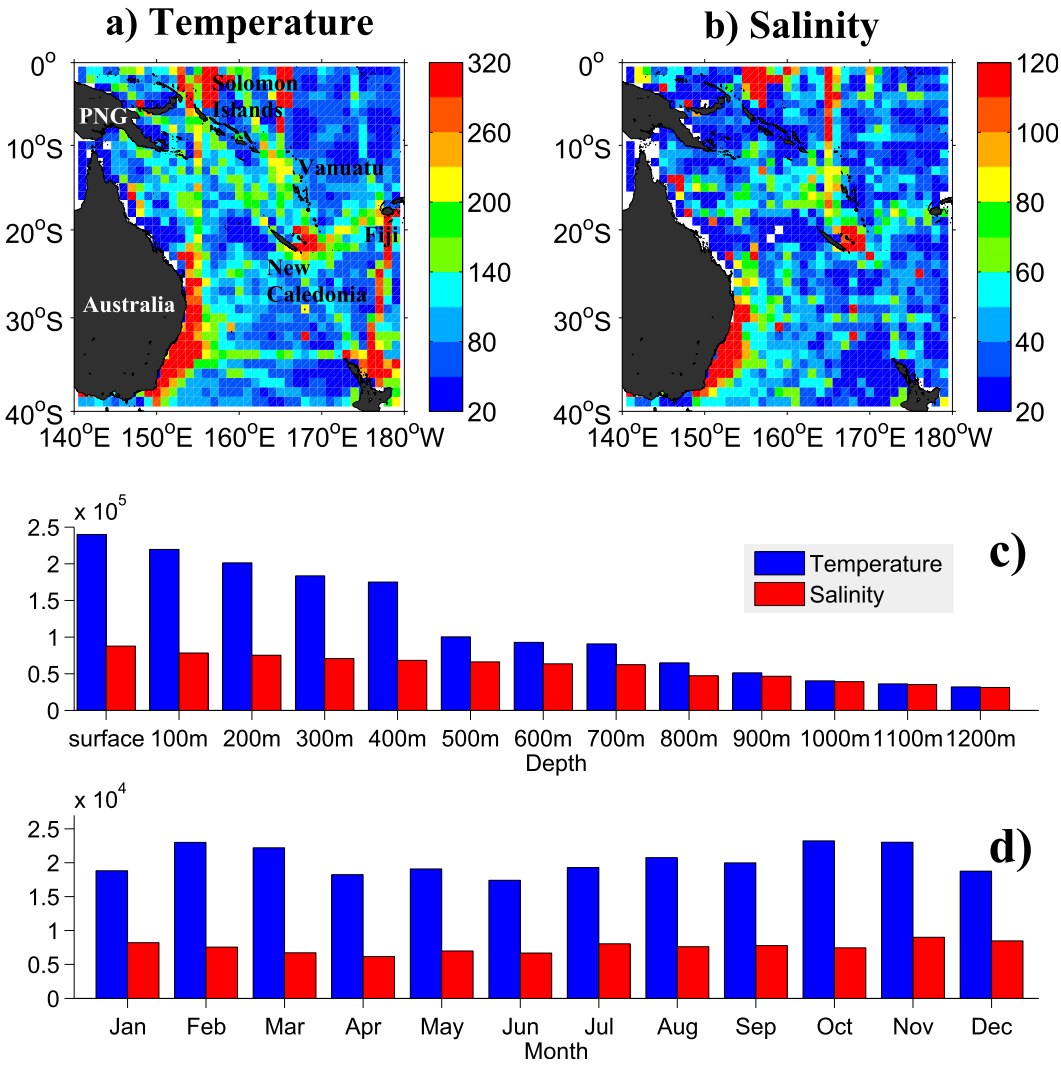

FIG. 1. Number of (a) temperature and (b) salinity profiles in 1° × 1° boxes of the southwest Pacific Ocean from WOD09. (c) Histogram of the temperature–salinity profiles observed in each level. (d) Histogram of the temperature–salinity profiles as a function of months.

It provides a general picture of the upper-layer circulation in the tropical southwest Pacific Ocean. Several major currents and jets including the EAC, GPC, North Vanuatu jet (NVJ), North Caledonian jet/South Caledonian jet (NCJ/SCJ), and North Fiji jet/South Fiji jet (NFJ/SFJ) can be identified, despite their seemingly weak magnitudes, which are probably due to smoothed horizontal filtering. The meridional component of velocity averaged within 2°-longitude bands over the upper 1000 m is presented in Fig. 2b. The basic structure of the bifurcation contour is close to that in Qu and Lindstrom (2002) and Kessler and Cravatte (2013), presenting a poleward shift with increasing depth, and it shares a similar pattern with those in the other oceans (Qu and Lukas 2003; Rodrigues et al. 2007; Chen et al. 2014). The detailed structure of the bifurcation, however, exhibits differently now that there are two zero contours with one extending from the surface to 1000 m and one bending from 400 to 1000 m. The discontinuity of the zero line may be attributed to the existence of the Marion Plateau, which makes the meridional component of the flow disconnect between 18° and 19°S. For the aforementioned reasons, in the rest of this study we only consider the SBL as the upper-layer (above $26.5\sigma_\theta$) mean to avoid pursuing an accurate position at each depth, which may blind us to its real seasonal cycle.

The mean SBL integrated over the upper 400 m is located between 17.5° and 17.8°S based on the calculations from WOD09 and ECCO2 but 15.5°S from the 20-yr altimetry SSH data analysis (Fig. 3). This 2° difference is largely because of the poleward tilting of the SEC bifurcation with increasing depth. In terms of the seasonal variation, the SBL moves to the southernmost

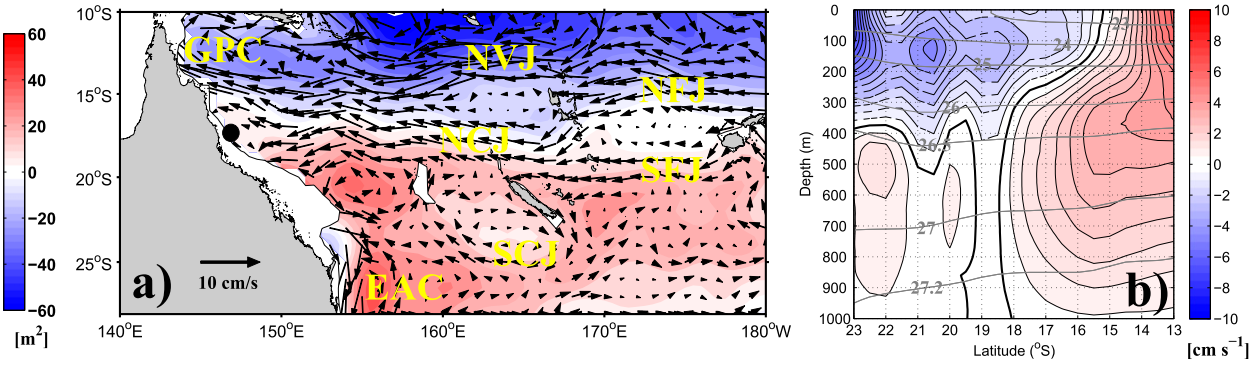

FIG. 2. (a) Mean depth-integrated (0–400 m) dynamic height relative to 1200 dbar. The mean dynamic height is removed. Yellow labels denote the main currents/jets. (b) Meridional geostrophic velocity (shaded) averaged within a 2°-longitude band off the Australian coast. The bold line indicates the SEC bifurcation, and the overlying gray contours are the potential density σ_θ calculated from the alongshore temperature–salinity data.

position in June/July and the northernmost position in November/December, with annual migration A_b of over 2.7°. The seasonal cycle of the SBL off the Australian coast is generally analogous to that in the NP, south Indian Ocean, and South Atlantic Ocean, all of which shift synchronously back and forth seasonally and arrive at their southernmost positions in boreal late spring and early summer (Qu and Lukas 2003; Rodrigues et al. 2007; Chen et al. 2014).

b. *Comparison with NEC bifurcation off the Philippine coast*

There are some striking contrasts between the seasonal cycles of the SEC/NEC bifurcation in the Pacific. It is shown in Fig. 4 that the SEC A_b is generally 2 times larger than its counterpart in the NP, that is, 2.7° versus 1.4° from the WOD09 geostrophic calculations, 3.6° versus 1.9° at the surface from satellite altimetry data analysis, and 2.9° versus 1.3° from ECCO2 meridional velocities. However, the zonally integrated, south–north annual excursion of the zero wind stress curl line A_w in the SP is comparable with, or even less than, that in the NP (8° vs 9°; Fig. 4d). This implies that, in addition to the SP/NP wind stress forcing, the SEC/NEC bifurcation may involve different processes in governing their seasonal variations, particularly the south–north annual migration. So the large difference in A_b motivates us to further investigate relevant processes in modulating the seasonal variation of the SEC bifurcation in the next section.

4. Role of Low-Lat-SP/Non-Low-Lat-SP processes in the SBL seasonal variation

a. *Modeling the SBL seasonal cycle*

It has been verified that the observed seasonal cycle of the NEC bifurcation off the Philippine coast can be well reproduced by both a linear Rossby wave propagation model (hereinafter referred to as the Rossby wave model) and 1.5-layer, nonlinear, reduced-gravity, primitive equation model (hereinafter referred to as the primitive equation model) (see Fig. 5a in Chen et al. 2014). In this study, we adopt the above-mentioned two models to simulate the seasonal cycle of the SEC bifurcation off the coast of Australia in the same manner.

The governing equations of the primitive equation model are

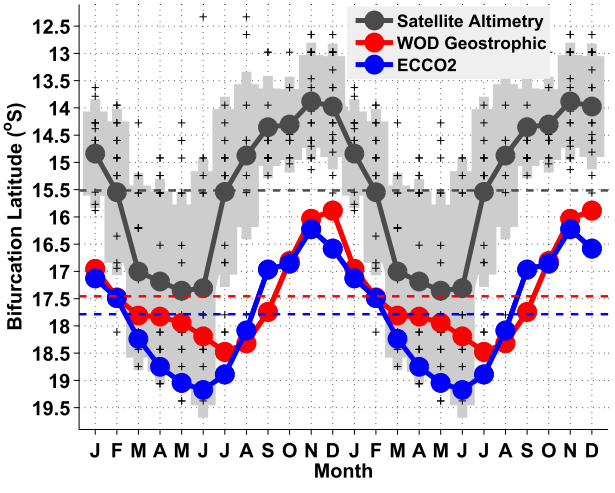

FIG. 3. Seasonal variation of the SBL derived from the satellite altimetry SSH data (black), the geostrophic flow averaged in the upper 400 m (red) derived from the WOD09 *T*–*S* data, and the meridional flow averaged in the upper 410 m from the ECCO2 product (blue). The pluses denote individual bifurcation latitudes estimated from the SSH data, and the shaded bars denote the standard deviation range. The dashed lines represent mean values.

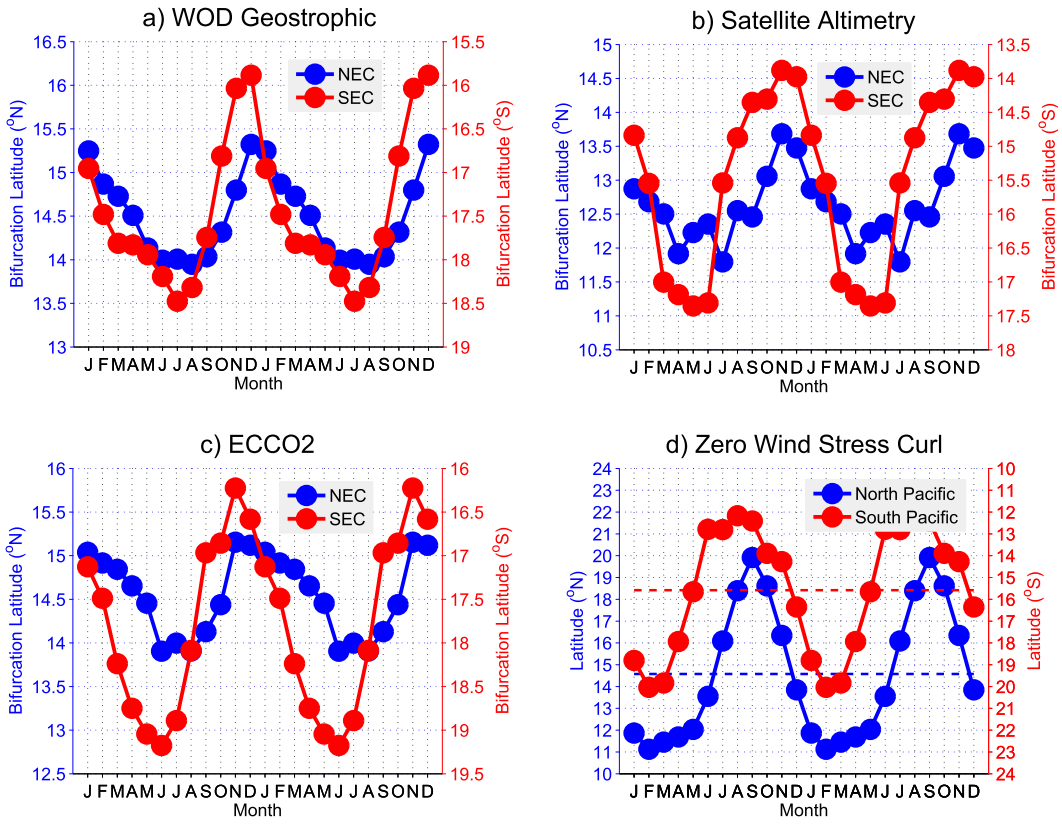

FIG. 4. Seasonal variations of the NEC/SEC bifurcation derived from (a) WOD09 geostrophic flow, (b) satellite altimetry, and (c) ECCO2 meridional velocities. (d) Seasonal evolution of the zonal-averaged latitude of zero wind stress curl line in both hemispheres.

$$\frac{\partial u}{\partial t}+u\frac{\partial u}{\partial x}+v\frac{\partial u}{\partial y}-fv+g'\frac{\partial h}{\partial x}=A_H\nabla^2 u+\frac{\tau^x}{\rho h}, \tag{1}$$

$$\frac{\partial v}{\partial t}+u\frac{\partial v}{\partial x}+v\frac{\partial v}{\partial y}+fu+g'\frac{\partial h}{\partial y}=A_H\nabla^2 v+\frac{\tau^y}{\rho h}, \quad \text{and} \tag{2}$$

$$\frac{\partial h}{\partial t}+\frac{\partial hu}{\partial x}+\frac{\partial hv}{\partial y}=0, \tag{3}$$

where u and v are the zonal and meridional velocity components, respectively; h is the upper-layer thickness; f is the Coriolis parameter; g' is the reduced-gravity acceleration; A_H is the coefficient of horizontal eddy viscosity ($2000\,\mathrm{m^2\,s^{-1}}$); ρ is the reference water density; and τ^x and τ^y are the surface wind stress. The primitive equation model covers the subtropical and tropical regions in the Pacific and Indian Oceans and extends from 45°S to 40°N in the meridional direction and from 20°E to 70°W in the zonal direction. The horizontal resolution of the model is 0.25°, and marginal seas shallower than 200 m are treated as land. We artificially made some modifications in the model topography, for example, the midocean islands except for New Caledonia, Vanuatu, and Fiji are eliminated; the Makassar Strait is the only passage that connects the two basins in the tropics.

The initial upper-layer thickness is $H = 350\,\mathrm{m}$. The density contrast between the abyssal ocean ($\rho = 1025\,\mathrm{kg\,m^{-3}}$) and the upper-layer ocean $\Delta\rho$ is $3\,\mathrm{kg\,m^{-3}}$, so g' in the model is $0.029\,\mathrm{m\,s^{-2}}$. No normal flow and nonslip boundary conditions are used along the coasts, and a free-slip condition is applied to the southern boundary at 45°S. Thus, there is no Antarctic Circumpolar Current (ACC) in the model but for a spurious zonal current due to the southern boundary condition.

The Rossby wave model is derived from the primitive equation, which governs the 1.5-layer ocean by adopting the long-wave approximation. The equation can be simply written as

$$\frac{\partial h}{\partial t}+C_R\frac{\partial h}{\partial x}=-\frac{1}{\rho_0 f}\nabla\times\boldsymbol{\tau}-\varepsilon h, \tag{4}$$

where C_R is the phase speed of first-mode baroclinic long Rossby wave; h is the anomaly of the upper-layer thickness; f is the Coriolis parameter; ρ_0 is the mean density of the upper-layer ocean; $\boldsymbol{\tau}$ is the wind stress vector; and ε is the Newtonian dissipation rate with the units of per year. In this study, we choose $\varepsilon = 0$ following

our recent study (Chen et al. 2014). Integrating (4) along the long Rossby wave characteristic line, we obtain

$$h(x,y,t)=\frac{1}{\rho_0 f}\int_{x_e}^{x}\frac{1}{C_R}\nabla\times\boldsymbol{\tau}\left(x',y,t-\frac{x-x'}{C_R}\right)dx'. \qquad (5)$$

In (5), we have ignored the part of the solution due to the eastern boundary forcing because its influence is limited to the eastern boundary, as reported in many studies like Fu and Qiu (2002) and Cabanes et al. (2006). Following Qiu and Lukas (1996), mass conservation requires the inflow at the western boundary to bifurcate where $h = 0$, so we define the SBL in the linear model at the position where the mean h within 2° off the western boundary is zero.

We use the monthly climatological wind stress/wind stress curl derived from the ERA-Interim reanalysis to force the primitive equation model (Control run) and the Rossby wave model. However, we get quite different SBL seasonal cycles (Fig. 5). The mean position simulated by the Rossby wave model is shifted northward by almost 2°, and A_b reduces by almost 0.5° with its peak season shifted earlier compared with observations, while the primitive equation model faithfully reproduces the observed SBL (recall Fig. 3).

With respect to the mean modeled SBL, it can be attributed to the fact that the Rossby wave model includes only the wind forcing in the Low-Lat-SP, that is, without an open ITF, while the primitive equation model allows it. Therefore, the Rossby wave/primitive equation model difference is simply because of the well-understood steady solution, and the mean position shift can be estimated by a steady, linear model [Godfrey's island rule; see the case for Madagascar in Chen et al. (2014)].

For their seasonal variations, the Rossby wave model fails to reproduce the observed season at its southernmost peak, implying the Rossby wave dynamic cannot adequately simulate the SBL seasonal cycle. A further model experiment (Linear run) clarifies that the effect of nonlinearity is very small, and it is not responsible for the difference in the seasonal cycles (dashed line in Fig. 5), so the disparity probably results from wind

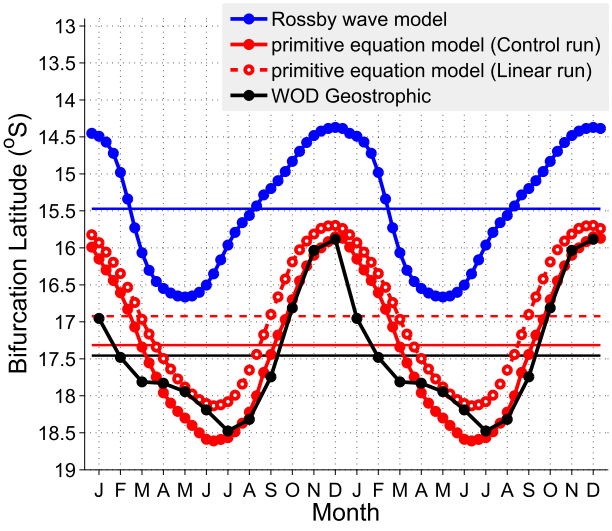

FIG. 5. Seasonal variation of the SBL derived from a Rossby wave model (blue), Control run (solid red line)/Linear run (dashed red line with open circles) by a primitive equation model and WOD09 geostrophic calculation (solid black line). The straight lines denote the mean values of respective seasonal cycles.

forcing in other regions and/or complex topography, which are all absent in the Rossby wave model. In the next part, we will conduct a series of sensitivity experiments using the primitive equation model to test and clarify the role of Low-Lat-SP/Non-Low-Lat-SP processes to further quantify their relative contributions in the seasonal variation of the SBL.

b. *Role of Low-Lat-SP processes: Rossby wave dynamics versus islands*

First, we check the Low-Lat-SP processes in the total variance of the SBL seasonal cycle. Here, we define the Low-Lat-SP as the region between the latitudes that the zero wind stress curl lines can reach at their respective southern/northern extremes (5°–30°S). To better illustrate the Low-Lat-SP processes, we applied the seasonally varying wind stress forcing in this region with mean wind forcing elsewhere (see the description of the sensitivity experiments in Table 1). Meanwhile, a parallel experiment is conducted to examine the impact of

TABLE 1. Sensitivity experiments conducted by the 1.5-layer, nonlinear, reduced-gravity, primitive equation model.

Name	Description of sensitivity experiments
Control run	Seasonal winds everywhere in the model domain.
Linear run	As in the Control run, but the nonlinear terms in the model are eliminated.
Low-Lat-SP run	Seasonal winds are applied within the region 30°–5°S, 140°E–70°W, with mean winds elsewhere.
Low-Lat-SP-noIs run	As in the Low-Lat-SP run, but the islands in the east of Coral Sea are artificially removed.
ITF run	Seasonal winds are applied within the region 10°S–10°N, 20°E–70°W, with mean winds elsewhere.
Non-Low-Lat-SP run	Opposite the Low-Lat-SP run, that is, mean winds are applied within the region 30°–5°S, 140°E–70°W, with seasonal winds elsewhere.

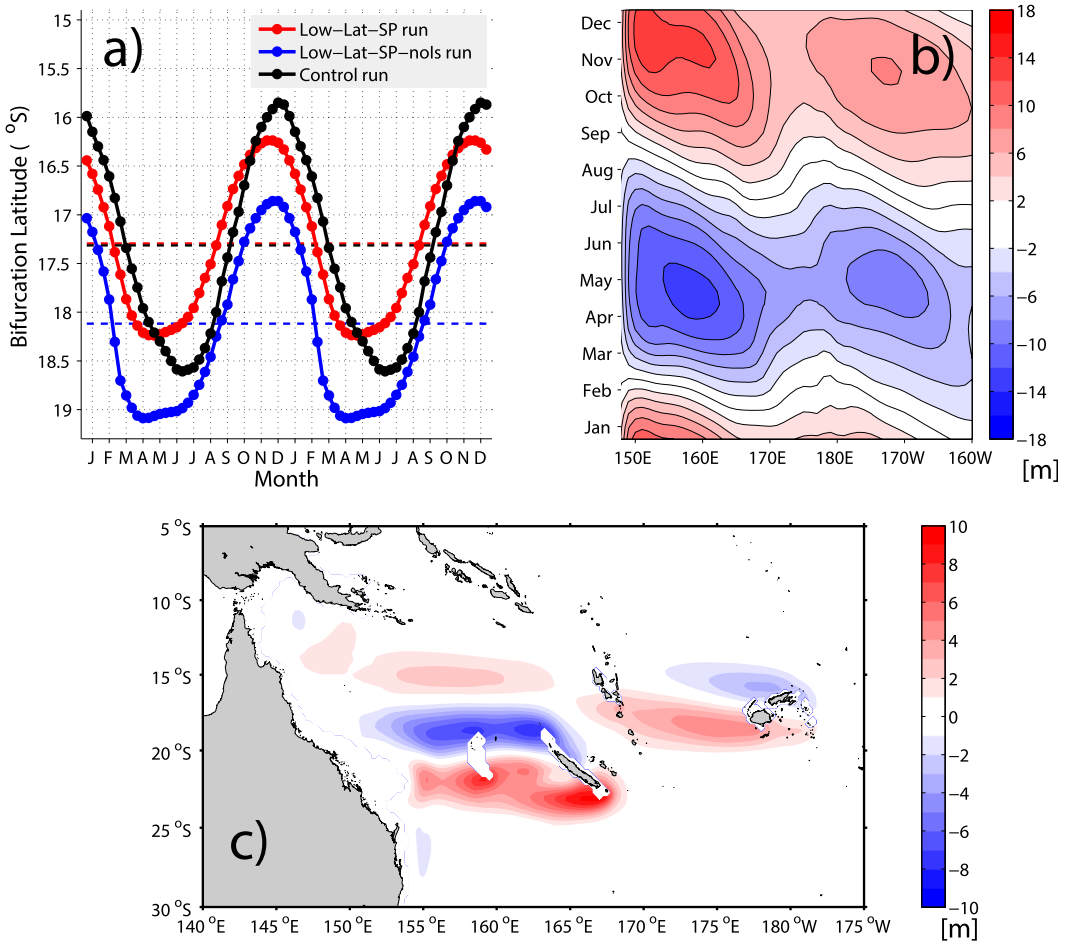

FIG. 6. (a) Seasonal variation of the SBL derived from the Low-Lat-SP run (red), Low-Lat-SP-noIs run (blue), and Control run (black). The dashed lines are the mean values of respective seasonal cycles. (b) Hövmoller diagram of ULT anomalies at 18°S calculated from the Low-Lat-SP-noIs run. (c) Spatial distribution of the difference in the seasonal amplitude of ULT between the two runs (Low-Lat-SP run minus Low-Lat-SP-noIs run).

islands (i.e., New Caledonia, Fiji, and Vanuatu) because they are believed to modulate the mean inflow significantly as the SEC enters the Coral Sea (Webb 2000; Gourdeau et al. 2008; Couvelard et al. 2008).

It is shown in Fig. 6a that both of these two cases yield distinct SBL seasonal cycles, which are analogous to the results from the Rossby wave model in terms of phase and A_b. Compared with the mean position predicted by the zero wind stress curl line, the simulated SBL are both shifted southward by over 2° because of the existence of the ITF in the primitive equation model. Moreover, the bifurcation moves farther southward as the islands are removed. This implies that the island obstacles, particularly New Caledonia, could reshape the incoming SEC into zonal jets to the southern/northern tip of the island (Ganachaud et al. 2008), thus leading to a northward bifurcation.

In addition to shifting the mean bifurcation latitude, the absence of these islands favors an amplified A_b (from 1.9° to 2.2°). We plot the Hövmoller diagram of the modeled upper-layer thickness (ULT) anomalies at 18°S in the Low-Lat-SP-noIs run and found these anomalies exhibit a distinct annual cycle in the Coral Sea; it deepens in November/December and shoals in April/May, consistent with the peak seasons of the modeled SBL (Fig. 6b). If the islands are taken into account, some of the incoming annual signals from the interior ocean would be damped or redistributed, leading to changes in ULT between New Caledonia and Australia. Spatial distribution of the difference in the seasonal amplitude of ULT between the above two runs indicates a reduced amplitude of ULT along NCJ paths and an enhanced amplitude along SCJ paths (Fig. 6c). Therefore, near the bifurcation, the amplitude of the pressure gradient annual cycle reduces, leading to reduced western boundary current anomaly, which favors the reduction of A_b.

It is worth noting that the seasonal cycle of the SBL in the absence of islands is identical to that in the Rossby

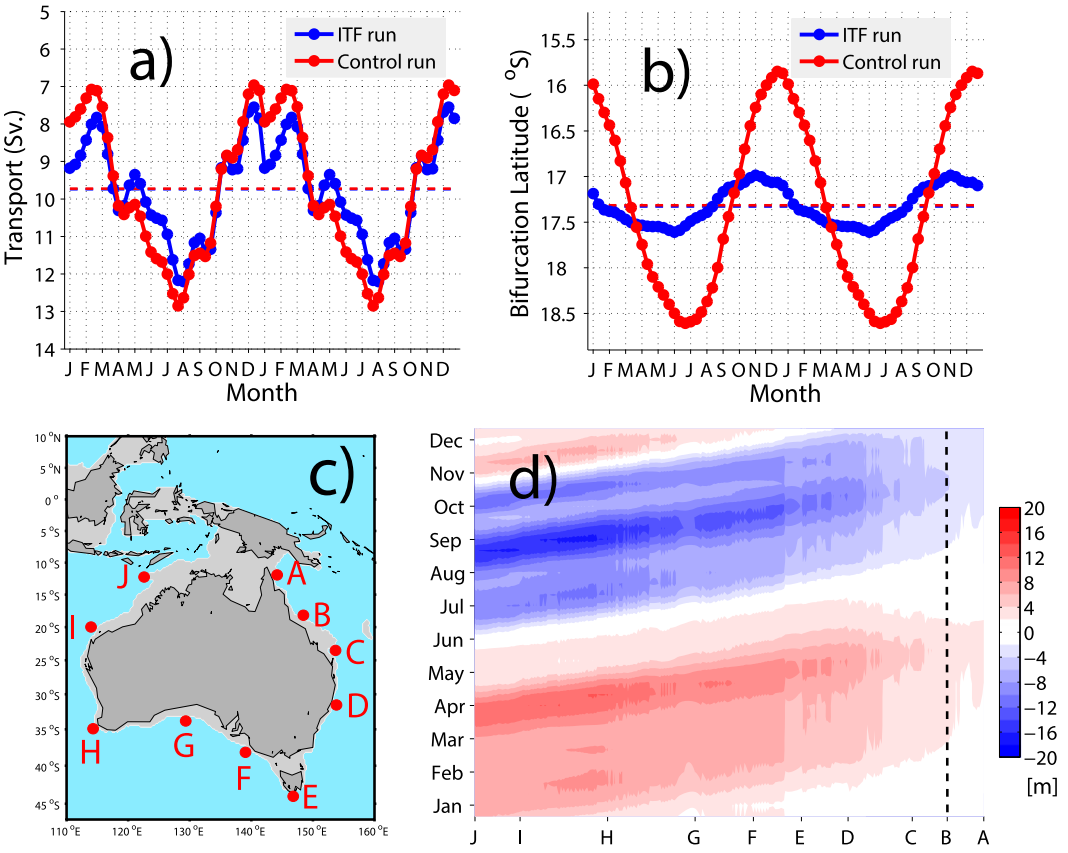

FIG. 7. Seasonal variation of (a) ITF transport and (b) SBL simulated by the primitive equation model [Control run (red), ITF run (blue)]. (c) Geographical locations of sampling points around Australian coast. (d) Hövmoller diagram of ULT anomalies along the western–southern–eastern portion of the Australian coast.

wave model in terms of phase and A_b (2.3° in the Rossby wave model and 2.2° in the primitive equation model), implying that the western boundary response to interior wind forcing is predominantly determined by the linear wave dynamics. The above analysis in the model indicates that the Rossby wave dynamics determine the basic feature of the SBL seasonal variation, while the islands in the east of the Coral Sea only work to reduce its annual range.

c. *Role of Non-Low-Lat-SP processes: ITF and alongshore winds*

The seasonally varying Low-Lat-SP winds in conjunction with the islands in the east of the Coral Sea produce an A_b of 1.9° but still fail to reproduce the total observed seasonal cycle as what the Control run has obtained. It raises the possibility of potential effects of processes out of the Low-Lat-SP region, for example, seasonally varying ITF, in regulating the SBL seasonal variation. Therefore, we set up an ITF run to examine its effect on the seasonal variation of the SBL. In this case, the seasonal wind forcing is only applied within the 10°S–10°N band because most of the ITF annual signal comes from the equatorial time-varying winds between 10°S and 10°N, particularly the equatorial Pacific winds (Potemra 1999). In addition, mean wind forcing is applied elsewhere to switch off the Rossby wave influences in the interior ocean.

It is demonstrated in Fig. 7a that the model captures the ITF transport in terms of its mean value and seasonal variability in both the Control run and ITF run, and it is consistent with recent observational and modeling studies (Potemra 1999; Sprintall et al. 2009). However, the annual range of the SBL exhibits only 0.6°, much smaller than that of Control run (Fig. 7b), explicitly indicating that the role of the seasonal ITF is minor compared to its significant effect of shifting the mean position. We further plot the time evolution of the modeled ULT anomalies along the Australian coast (see the coastal sites in Fig. 7c), and it is indicated that the annual reversed signals that are generated by the equatorial winds propagate anticlockwise, taking one and a half months to reach the eastern coast (Fig. 7d). These signals, also called the coastal Kelvin waves

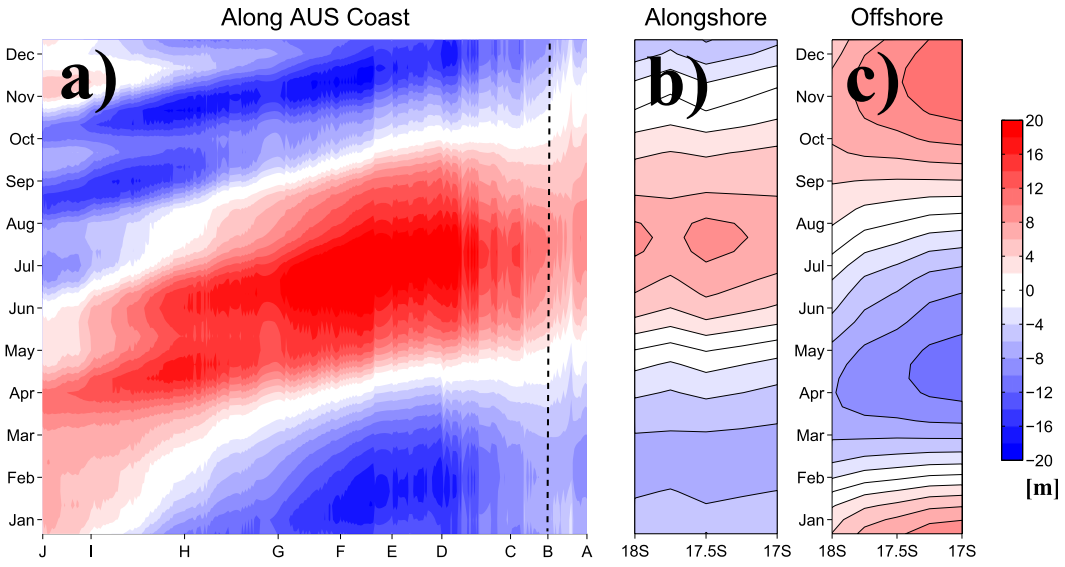

FIG. 8. (a) Hövmoller diagram of ULT anomalies along the western–southern–eastern portion of the Australian coast. The dashed line denotes the mean position of the modeled bifurcation. (b) ULT anomalies within 50 km along the east coast of Australia between 17° and 18°S. (c) As in (b), but for the ULT anomalies of 100 km offshore.

(CKWs), are continuously damped along their path because of dissipation, particularly off the east coast of Australia. Therefore, as can be seen in Fig. 7d, these signals only exert seasonal amplitude of about 2–3 m, leading to weak modulations on the annual range of the SBL (Fig. 7b).

The CKWs in the ITF run provide a link between the seasonal change in ULT along the western coast of Australia and the alongshore pressure change in the SEC bifurcation region. This further signifies an important role of alongshore winds around Australia, which could potentially enhance the alongshore pressure via both local Ekman transport/pumping along with the upstream CKWs. To confirm this, we plot the time evolution of the modeled ULT anomalies along the Australian coast derived from the Control run in Fig. 8a. Compared with the ITF run, the seasonal amplitude of ULT is enhanced along the Australian coast in the presence of the alongshore winds, particularly the westerlies along the long south coast. Although these signals are quite damped along the east coast, there are still significant ULT anomalies (~10 m) near the bifurcation region (Fig. 8b). In the Control run, where the Low-Lat-SP winds are involved, the offshore ULT near bifurcation varies seasonally but out of phase with the alongshore ULT. This is mainly because of the lagged baroclinic adjustment of the ULT to the basinwide wind forcing (Chen and Qiu 2004). Therefore, the phase mismatching between alongshore and offshore ULT will result in a large zonal pressure gradient at the western boundary, with large flow anomalies (i.e., EAC and GPC) near the bifurcation favoring an amplified A_b.

d. *Seasonal cycle of the SBL: Combined effect of Low-Lat-SP and Non-Low-Lat-SP processes*

We have shown that both Low-Lat-SP winds and Non-Low-Lat-SP winds are responsible for the seasonal variation of the SBL in the Control run. To quantify their contributions to the total variance of the SBL, we conduct a Non-Low-Lat-SP run to turn off the Low-Lat-SP processes that are predominantly governed by Rossby wave dynamics. Figure 9 explicitly demonstrates

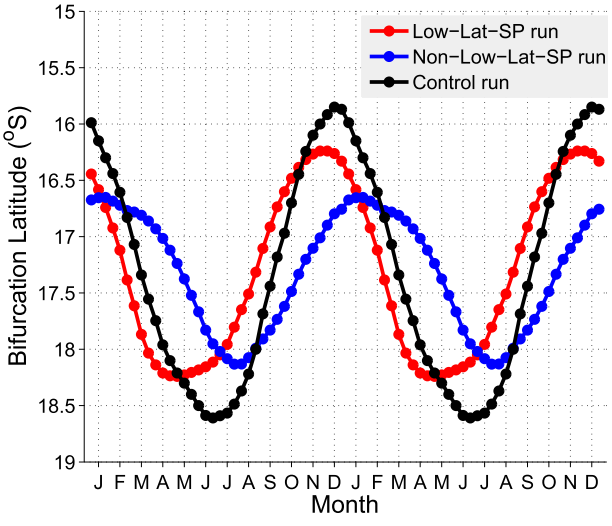

FIG. 9. Seasonal variation of the SBL derived from the Low-Lat-SP run (red), Non-Low-Lat-SP run (blue), and the Control run (black).

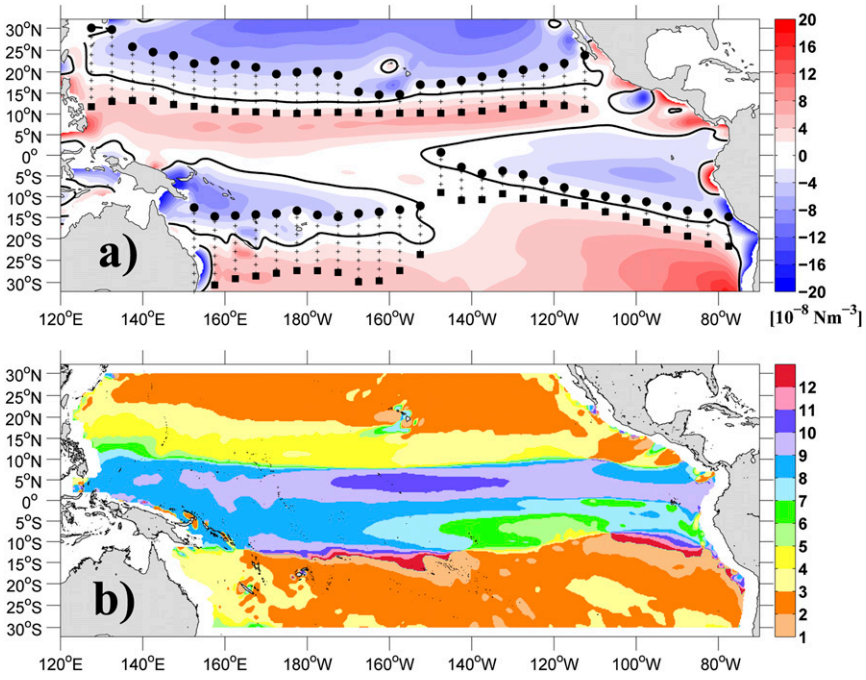

FIG. 10. (a) Map of mean wind stress curl (shaded) and southernmost/northernmost position of zero wind stress curl line at different longitudes during a year. (b) Peak seasons of wind stress curl after annual harmonic (month of minimum curl).

the seasonal cycles of the SBL determined by the above-mentioned two processes. It is shown that each seasonal cycle resembles the total observed/simulated SBL seasonal cycle but with slight phase shift and amplitude reduction. We calculated the explained variance of each seasonal cycle to the total SBL in terms of skill s following Qiu (2002). The skill is defined by $s = 1 - \langle(\mathrm{SBL_{Ctrl}} - \mathrm{SBL_{Sen}})^2\rangle / \langle \mathrm{SBL^2_{Ctrl}} \rangle$, where $\mathrm{SBL_{Ctrl}}$ is the SBL time series derived from the Control run, $\mathrm{SBL_{Sen}}$ is the SBL time series derived from each sensitivity run, and the angle brackets denote time averaging. The skill of the Low-Lat-SP run is $s = 0.79$, while the Non-Low-Lat-SP run is $s = 0.49$. Therefore, the Low-Lat-SP process independently explains 79% of the total variance of the observed/simulated SBL, while the Non-Low-Lat-SP process independently explains 49%. The total annual range of the SBL (2.8°) cannot be obtained directly by linear superposition (1.9° vs 1.4°) because the peak seasons in both runs do not match each other (recall Figs. 8b,c). Thus, the Low-Lat-SP process (referred to as the Rossby wave dynamics forced by the wind stress curl over the SP) accounts for almost ⅔ of the SBL seasonal variability, and the Non-Low-Lat-SP processes account for ⅓.

Here, we highlight the combined effect from the two processes in modulating the seasonal variation of the SBL. The Low-Lat-SP wind forcing determines the offshore ULT via Rossby wave propagation and island regulation, while the Non-Low-Lat-SP wind forcing determines the alongshore ULT via alongshore winds and CKWs propagation. This is the most essential difference between the seasonal variation of the SBL and the NBL. Alongshore winds are of minor importance around the Philippine coast, so the Rossby wave model can adequately simulate the observed seasonal cycle of the NEC bifurcation.

5. A simple model of seasonal SEC/NEC bifurcation

The analysis in the above sections has clarified that the seasonal variation of the SEC bifurcation is more complicated compared to the NEC bifurcation due to alongshore winds and the ITF. However, regardless of the Non-Low-Lat-SP processes, there still exists a large disparity in A_b (2.3° vs 1.4°) in a Rossby wave model that is only forced by low-latitude winds in both hemispheres (Fig. 5 in this paper and Fig. 5a in Chen et al. 2014), so it is helpful to explore the cause of the difference in depth.

Considering that the zonally integrated A_w in the SP is comparable to that in the NP (Fig. 4d), the large disparity in A_b raises the potential role of spatial nonuniform wind stress curl that may lead to incorrect estimations of A_b by the zonally integrated A_w. Figure 10 demonstrates the

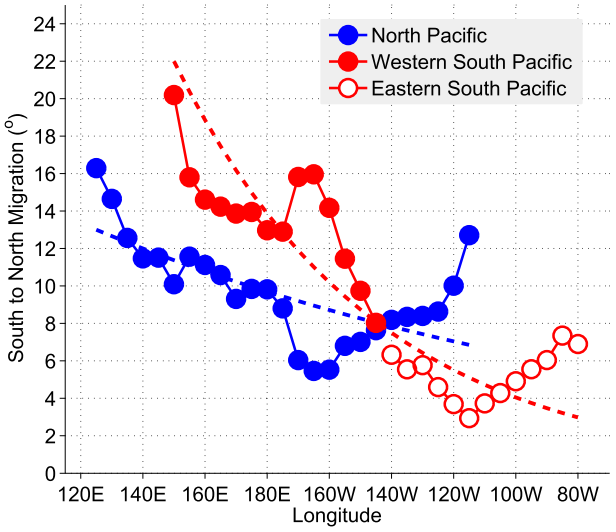

FIG. 11. South–north migration of zero wind stress curl line as a function of longitude. The red open/solid circles denote A_w in the western/eastern SP. The dashed lines are exponential fits of them.

southernmost/northernmost position of the zero curl line during a year and the peak seasons of wind stress curl. The most striking feature in Fig. 10a is the disconnected zero line in the SP and A_w in the eastern SP is close to zero. This indicates the weak amplitude of curl in the eastern SP, while the annual north–south excursion of west Pacific trades is large (Kessler and Gourdeau 2007). On the contrary, in the NP, A_w is almost the same from east to west except for the Hawaiian regions, where persistent small-scale ocean winds are dominant (Chelton et al. 2004). Another feature in Fig. 10b is the in-phase changes of the wind stress curl over the Low-Lat-SP/NP regions, indicating the synchronous shift of zero lines during a year.

Given the overall spatial pattern of the wind stress curl, we introduce in this study a simple model to estimate the seasonal cycle of the bifurcation under the framework of linear Rossby wave dynamics. Here, we regard the bifurcation as the total response at the western boundary to the south–north migration of the zero wind stress curl line. Since it generally reaches its southernmost position in February/March, the zero line migration during a year F can be simply expressed by

$$F(t) = -A\sin(\omega t), \tag{6}$$

where A is half of A_w, $\omega = 2\pi/T_0$, and T_0 is the annual period. To better illustrate the wind pattern in this simple model, we use exponential curve fitting to represent A_w because it varies with space in both hemispheres. It is shown in Fig. 11 that A_w in both hemispheres exhibits a decreasing trend from west to east, comparable with the curl amplitude shown in Kessler and Gourdeau (2007). The expression of the wind forcing at x becomes

$$F(x,t) = Ae^{-(x/kL)}\cos\left(\omega t + \frac{\pi}{2}\right), \tag{7}$$

where k describes the spatial pattern of wind, and L is the basin width. Here, k is 1.5 for the NP and 0.5 for the SP.

Analogous to the Rossby wave model, it is assumed that all signals excited at any location can propagate freely to reach the western boundary. Thus, the response r at the western boundary to any wind forcing at x is

$$r(x,t) = Ae^{-(x/kL)}\cos\left(\omega t + \frac{\pi}{2} - \omega\frac{x}{c}\right), \tag{8}$$

where c is the phase speed of the first-mode baroclinic Rossby wave. The total response R to basin-scale wind forcing can be expressed as the integration of r from the western boundary ($x = 0$) to the eastern boundary ($x = L$):

$$\begin{aligned} R(t) &= \frac{1}{L}\int_0^L r(x,t)\,dx \\ &= \frac{1}{L}\int_0^L Ae^{-(x/kL)}\cos\left(\omega t + \frac{\pi}{2} - \omega\frac{x}{c}\right)dx \\ &= A\frac{cke^{-(1/k)}}{c^2 + k^2L^2\omega^2}\left\{-kL\omega\cos\left(\omega t - \omega\frac{L}{c}\right)\right. \\ &\quad \left. + e^{(1/k)}[kL\omega\cos(\omega t) - c\sin(\omega t)] + c\sin\left(\omega t - \omega\frac{L}{c}\right)\right\}. \end{aligned} \tag{9}$$

Here, we introduce a parameter ε, which is called the baroclinic adjustment coefficient. It is defined as

$$\varepsilon = \frac{c}{\omega L} = \frac{1}{2\pi a}, \tag{10}$$

where a is the transit years for the first-mode baroclinic Rossby wave crossing the entire basin. For the low-latitude Pacific Ocean, the transit years are generally 3–5 yr at the latitude of SEC/NEC bifurcation, so ε is much less than $O(0.1)$. Substituting ε in (9), we have

$$\begin{aligned} R(t) = \frac{\varepsilon}{(\varepsilon/k)^2 + 1}A\left[\cos(\omega t) - e^{-(1/k)}\cos(\omega t - 2\pi a)\right. \\ \left. -\frac{\varepsilon}{k}\sin(\omega t) + \frac{\varepsilon}{k}e^{-(1/k)}\sin(\omega t - 2\pi a)\right]. \end{aligned} \tag{11}$$

This is the most meaningful expression for the western boundary response to the interior wind forcing. The

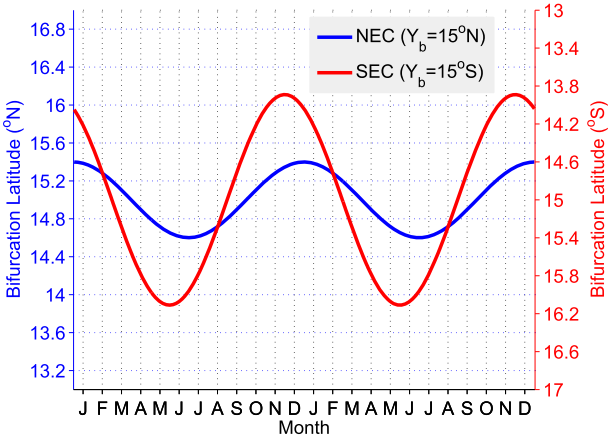

FIG. 12. Seasonal cycle of NBL/SBL derived from the simple bifurcation model.

term in front of A is defined as the damping coefficient, which is determined by the baroclinic Rossby wave propagation in terms of ε as well as the spatial pattern of wind in terms of k. Physically speaking, most of the annual wind migration signals are cancelled as they propagate westward so that A_b is generally $O(0.1)$ of A_w. The terms in the brackets set up the phase for the response; that is, the first term indicates the response to local wind forcing ($x = 0$), and the second term is the response to remote wind forcing ($x = L$). The third and fourth terms are all of high order, exerting little effect compared with the first two terms. Eliminating the third and fourth terms, we obtain a simple expression for the bifurcation latitude $Y(t)$:

$$Y(t) = \frac{\varepsilon}{(\varepsilon/k)^2 + 1} A[\cos(\omega t) - e^{-(1/k)}\cos(\omega t - 2\pi a)] + \text{MeanLat(zero curl)}. \tag{12}$$

It is worth noting that the magnitude of the remote forcing term, despite its lag of $2\pi a$, is always smaller than the local forcing term because the term $e^{-(1/k)}$ is less than 1 (recall that k equals to 1.5/0.5 in the NP/SP). So it can be inferred that the phase of the bifurcation mainly follows the local forcing term with $\pi/2$ lag, that is, the seasonal cycle of the SEC/NEC bifurcation generally reaches its southernmost position in May/June as the zero wind stress curl line reaches its southernmost position in February/March.

Assuming the SEC/NEC bifurcates at 15°S/15°N, the phase speed of the first-mode baroclinic Rossby wave is $0.16\,\mathrm{m\,s^{-1}}$. Considering that the eastern part of the SP wind forcing is negligible, we derived the seasonal cycle of the SBL/NBL using (12) according to the related parameters in Fig. 11, that is, $A = 6.5°$ (11°) and $k = 1.5$ (0.5) in the NP (SP). It is shown in Fig. 12 that this simple model well produced the seasonal cycles of the SEC/NEC bifurcation under the framework of linear Rossby wave dynamics, suggesting a basic understanding on the seasonal variation of the global equatorial current bifurcation, as well as the western boundary transport in the low-latitude ocean.

6. Summary and discussion

In this study, we have investigated the seasonal variation of the South Equatorial Current (SEC) bifurcation off the Australian coast in the upper South Pacific (SP) with observations and a 1.5-layer, nonlinear, reduced-gravity, primitive equation model. The mean SBL integrated over the upper thermocline is around 17.5°S, which is almost 2° south of the position predicted by Sverdrup theory. As in the peak seasons in the North Pacific, south Indian Ocean, and South Atlantic Ocean, the SEC bifurcation in the SP shifts synchronously back and forth seasonally and reaches its southernmost position in June/July and northernmost in November/December.

Further comparisons between the seasonal cycles of the SEC and NEC bifurcation indicate that the SEC/NEC bifurcations are different, particularly in terms of the south–north annual migrations; the south–north migration of 2.7° in the SP is twice as large as its counterpart in the North Pacific. A series of numerical experiments using the 1.5-layer, nonlinear, reduced-gravity, primitive equation model have clarified that the large SEC A_b is attributed to the combined effect of Low-Lat-SP and Non-Low-Lat-SP processes. The Low-Lat-SP process (referred to as the Rossby wave dynamics forced by the wind stress curl over the SP) accounts for almost ⅔ of the SBL seasonal variability, and the Non-Low-Lat-SP processes account for ⅓. Both of these processes are responsible for its south–north migration but in different ways. The Low-Lat-SP wind forcing determines the ULT via Rossby wave propagation, while the Non-Low-Lat-SP wind forcing determines the alongshore ULT via coastal Kelvin waves propagation.

The above governing processes are, to some extent, similar to that in explaining the seasonal SEC bifurcation off the coast of Madagascar (Chen et al. 2014). Both cases highlight the role of an isolated island, that is, Madagascar and the Australia–Papua continent, in modulating the mean positions and seasonal cycles of the SEC bifurcation. However, the time-dependent island rule (TDIR), which is proven to work well for the seasonal SBL off the coast of Madagascar, does not properly model the seasonal cycle of the SBL off the coast of Australia. On one hand, the TDIR model

cannot take into account the existence of the islands in the east of Coral Sea, as suggested in this study; on the other hand, the circum-island transport induced by the alongshore winds cannot be analytically evaluated because it takes one and a half months to adjust the anomalies around the Australian–Papua continent from the west to east coast in terms of coastal Kelvin waves. Furthermore, the waves cannot pass completely around the Australian–Papua continent because it extends just past the equator (Kessler and Gourdeau 2007), whereas this kind of circum-island response is regarded as instantaneous in the Madagascar case.

Apart from the Non-Low-Lat-SP processes, we introduce here a simple bifurcation model involving the interior wind stress forcing in conjunction with a baroclinic adjustment process. The seasonal variation of the bifurcation latitude is predominantly determined by the spatial pattern of the wind and baroclinic Rossby wave propagation. This model works well in the seasonal cycles of the SEC/NEC bifurcation under different spatial wind forcing in both hemispheres and provides a practical way to understand the role of local/remote wind forcing and baroclinic adjustment in its south–north migration and peak seasons.

The simple bifurcation model has extended the theoretical solution that was put forth by Qiu and Lukas (1996), who applied the zonally integrated wind stress curl to force the linear Rossby wave model. The absence of the wind spatial pattern in their model, as a consequence, resulted in a highly sensitive solution to the choice of phase speed of the Rossby wave, which may lead to an incorrect phase of the seasonal cycle. This is also the case for this simple model as k approaches infinity, (12) becomes

$$\begin{aligned} Y(t) &= \varepsilon A[\cos(\omega t) - \cos(\omega t - 2\pi a)] + \text{MeanLat(curl)} \\ &= -2\varepsilon A \sin(\pi a)\sin(\omega t - \pi a) + \text{MeanLat(curl)}, \end{aligned} \tag{13}$$

which means the amplitude and phase of the seasonal bifurcation fully depends on the transit years of the Rossby wave. This may explain why the NEC A_b increased at first and then decreased with increasing wave speed because of the equatorward shift over the past 60 yr, as suggested by Chen and Wu (2012). Meanwhile, in the SP, A_w decreases exponentially away from the western boundary, which implies that the SEC A_b will increase continuously with accelerating wave speed due to a more stratified upper ocean.

Acknowledgments. This study is inspired by the innovative works of Qiu and Lukas (1996) and Kessler and Gourdeau (2007). We benefited from discussions with Bo Qiu, Peter Rhines, Tangdong Qu, William Kessler, Awnesh Singh, and Shantong Sun. We thank two anonymous reviewers for their constructive comments. We thank Michael Spall, Doug Koch, and Honghai Zhang for improving the early version of the manuscript. We are also indebted to the CLS Space Oceanography Division for providing us the merged satellite altimeter data. This research is supported by the National Science Foundation of China (41306001, 41221063, and U1406401), the National Basic Research Program of China (2013CB956200), China Postdoctoral Science Foundation (2013M540564), Global Change Project (GASI-03-01-01-05), and Open Fund of the Key Laboratory of Ocean Circulation and Waves (KLOCAW1306).

REFERENCES

Boyer, T. P., and Coauthors, 2009: *World Ocean Database 2009.* NOAA Atlas NESDIS 66, 216 pp.

Burrage, D., and Coauthors, 2012: Naming a western boundary current from Australia to the Solomon Sea. *CLIVAR Exchanges,* No. 58, International CLIVAR Project Office, Southampton, United Kingdom, 28.

Cabanes, C., T. Huck, and A. C. D. Verdiere, 2006: Contributions of wind forcing and surface heating to interannual sea level variation in the Atlantic Ocean. *J. Phys. Oceanogr.,* **36,** 1739–1750, doi:10.1175/JPO2935.1.

Chelton, D. B., M. G. Schlax, M. H. Freilich, and R. F. Milliff, 2004: Satellite measurements reveal persistent small-scale features in ocean winds. *Science,* **303,** 978–983, doi:10.1126/science.1091901.

Chen, S., and B. Qiu, 2004: Seasonal variability of the South Equatorial Countercurrent. *J. Geophys. Res.,* **109,** C08003, doi:10.1029/2003JC002243.

Chen, Z., and L. Wu, 2011: Dynamics of the seasonal variation of the North Equatorial Current bifurcation. *J. Geophys. Res.,* **116,** C02018, doi:10.1029/2010JC006664.

——, and ——, 2012: Long-term change of the Pacific North Equatorial Current bifurcation in SODA. *J. Geophys. Res.,* **117,** C06016, doi:10.1029/2011JC007814.

——, ——, B. Qiu, S. Sun, and F. Jia, 2014: Seasonal variation of the South Equatorial Current bifurcation off Madagascar. *J. Phys. Oceanogr.,* **44,** 618–630, doi:10.1175/JPO-D-13-0147.1.

Church, J. A., 1987: The East Australian Current adjacent to the Great Barrier Reef. *Aust. J. Mar. Freshwater Res.,* **38,** 671–683, doi:10.1071/MF9870671.

Couvelard, X., P. Marchesiello, L. Gourdeau, and J. Lefebvre, 2008: Barotropic zonal jets induced by islands in the southwest Pacific. *J. Phys. Oceanogr.,* **38,** 2185–2204, doi:10.1175/2008JPO3903.1.

De Szoeke, R. A., 1987: On the wind-driven circulation of the South Pacific Ocean. *J. Phys. Oceanogr.,* **17,** 613–630, doi:10.1175/1520-0485(1987)017<0613:OTWDCO>2.0.CO;2.

Fu, L.-L., and B. Qiu, 2002: Low-frequency variability of the North Pacific Ocean: The roles of boundary- and wind-driven baroclinic Rossby waves. *J. Geophys. Res.,* **107,** 3220, doi:10.1029/2001JC001131.

Ganachaud, A., and Coauthors, 2007: Southwest Pacific Ocean Circulation and Climate Experiment (SPICE)—Part I. Scientific

background. CLIVAR Publication Series 111, NOAA/OAR Special Rep., 37 pp. [Available online at www.pmel.noaa.gov/pubs/PDF/gana3070/gana3070.pdf.]

——, L. Gourdeau, and W. S. Kessler, 2008: Bifurcation of the subtropical South Equatorial Current against New Caledonia in December 2004 from a hydrographic inverse box model. *J. Phys. Oceanogr.,* **38,** 2072–2084, doi:10.1175/2008JPO3901.1.

Gourdeau, L., W. S. Kessler, R. E. Davis, J. Sherman, C. Maes, and E. Kestenare, 2008: Zonal jets entering the Coral Sea. *J. Phys. Oceanogr.,* **38,** 715–725, doi:10.1175/2007JPO3780.1.

Jensen, T. G., 2011: Bifurcation of the Pacific North Equatorial Current in a wind-driven model: Response to climatological winds. *Ocean Dyn.,* **61,** 1329–1344, doi:10.1007/s10236-011-0427-2.

Kessler, W. S., and L. Gourdeau, 2007: The annual cycle of circulation of the southwest subtropical Pacific, analyzed in an ocean GCM. *J. Phys. Oceanogr.,* **37,** 1610–1627, doi:10.1175/JPO3046.1.

——, and S. Cravatte, 2013: Mean circulation of the Coral Sea. *J. Geophys. Res. Oceans,* **118,** 6385–6410, doi:10.1002/2013JC009117.

Kim, Y. Y., T. Qu, T. Jensen, T. Miyama, H. Mitsudera, H.-W. Kang, and A. Ishida, 2004: Seasonal and interannual variation of the North Equatorial Current bifurcation in a high-resolution OGCM. *J. Geophys. Res.,* **109,** C03040, doi:10.1029/2003JC002013.

McCreary, J. P., T. Miyama, R. Furue, T. Jensen, H.-W. Kang, B. Bang, and T. Qu, 2007: Interactions between the Indonesian Throughflow and circulations in the Indian and Pacific Oceans. *Prog. Oceanogr.,* **75,** 70–114, doi:10.1016/j.pocean.2007.05.004.

Menemenlis, D., J. M. Campin, P. Heimbach, C. Hill, T. Lee, A. Nguyen, M. Schodlok, and H. Zhang, 2008: ECCO2: High resolution global ocean and sea ice data synthesis. *Mercator Ocean Quarterly Newsletter,* No. 31, Mercator-Océan, Ramonville Saint-Agne, France, 13–21.

Potemra, J. T., 1999: Seasonal variations of upper ocean transport from the Pacific to the Indian Ocean via Indonesian straits. *J. Phys. Oceanogr.,* **29,** 2930–2944, doi:10.1175/1520-0485(1999)029<2930:SVOUOT>2.0.CO;2.

Qiu, B., 2002: Large-scale variability in the midlatitude subtropical and subpolar North Pacific Ocean: Observations and causes. *J. Phys. Oceanogr.,* **32,** 353–375, doi:10.1175/1520-0485(2002)032<0353:LSVITM>2.0.CO;2.

——, and R. Lukas, 1996: Seasonal and interannual variability of the North Equatorial Current, the Mindanao Current, and the Kuroshio along the Pacific western boundary. *J. Geophys. Res.,* **101,** 12 315–12 330, doi:10.1029/95JC03204.

——, D. L. Rudnick, S. Chen, and Y. Kashino, 2013: Quasi-stationary North Equatorial Undercurrent jets across the tropical North Pacific Ocean. *Geophys. Res. Lett.,* **40,** 2183–2187, doi:10.1002/grl.50394.

Qu, T., and E. Lindstrom, 2002: A climatological interpretation of the circulation in the western South Pacific. *J. Phys. Oceanogr.,* **32,** 2492–2508, doi:10.1175/1520-0485-32.9.2492.

——, and R. Lukas, 2003: The bifurcation of the North Equatorial Current in the Pacific. *J. Phys. Oceanogr.,* **33,** 5–18, doi:10.1175/1520-0485(2003)033<0005:TBOTNE>2.0.CO;2.

Ridgway, K. R., and J. S. Godfrey, 1997: Seasonal cycle of the East Australian Current. *J. Geophys. Res.,* **102,** 22 921–22 936, doi:10.1029/97JC00227.

——, and J. R. Dunn, 2003: Mesoscale structure of the East Australian Current system and its relationship with topography. *Prog. Oceanogr.,* **56,** 189–222, doi:10.1016/S0079-6611(03)00004-1.

Rio, M. H., S. Guinehut, and G. Larnicol, 2011: New CNES-CLS09 global mean dynamic topography computed from the combination of GRACE data, altimetry, and in situ measurements. *J. Geophys. Res.,* **116,** C07018, doi:10.1029/2010JC006505.

Rodrigues, R. R., L. M. Rothstein, and M. Wimbush, 2007: Seasonal variability of the South Equatorial Current bifurcation in the Atlantic Ocean: A numerical study. *J. Phys. Oceanogr.,* **37,** 16–30, doi:10.1175/JPO2983.1.

Sprintall, J., S. E. Wijffels, R. Molcard, and I. Jaya, 2009: Direct estimates of the Indonesian Throughflow entering the Indian Ocean: 2004–2006. *J. Geophys. Res.,* **114,** C07001, doi:10.1029/2008JC005257.

Tsuchiya, M., R. Lukas, R. A. Fine, E. Firing, and E. Lindstrom, 1989: Source waters of the Pacific Equatorial Undercurrent. *Prog. Oceanogr.,* **23,** 101–147, doi:10.1016/0079-6611(89)90012-8.

Wang, Q., and D. Hu, 2006: Bifurcation of the North Equatorial Current derived from altimetry in the Pacific Ocean. *J. Hydrodyn.,* **18,** 620–626, doi:10.1016/S1001-6058(06)60144-3.

Webb, D. J., 2000: Evidence for shallow zonal jets in the South Equatorial Current region of the southwest Pacific. *J. Phys. Oceanogr.,* **30,** 706–720, doi:10.1175/1520-0485(2000)030<0706:EFSZJI>2.0.CO;2.